The *Hubble Space Telescope* PanCET Program: Exospheric Mg II and Fe II in the Near-ultraviolet Transmission Spectrum of WASP-121b Using Jitter Decorrelation

David K. Sing[1,2] , Panayotis Lavvas[3] , Gilda E. Ballester[4], Alain Lecavelier des Etangs[5], Mark S. Marley[6] , Nikolay Nikolov[1], Lotfi Ben-Jaffel[5], Vincent Bourrier[7] , Lars A. Buchhave[8] , Drake L. Deming[9], David Ehrenreich[7] , Thomas Mikal-Evans[10] , Tiffany Kataria[11], Nikole K. Lewis[12] , Mercedes López-Morales[13] , Antonio García Muñoz[14] , Gregory W. Henry[15] , Jorge Sanz-Forcada[16] , Jessica J. Spake[17], and Hannah R. Wakeford[18]

(The PanCET collaboration)

[1] Department of Earth & Planetary Sciences, Johns Hopkins University, Baltimore, MD, USA; dsing@jhu.edu
[2] Department of Physics & Astronomy, Johns Hopkins University, Baltimore, MD, USA
[3] Groupe de Spectrométrie Moléculaire et Atmosphérique, Université de Reims, Champagne-Ardenne, CNRS UMR 7331, France
[4] Lunar and Planetary Laboratory, University of Arizona, Tucson, AZ 85721, USA
[5] Sorbonne Universités, UPMC Université Paris 6 and CNRS, UMR 7095, Institut d'Astrophysique de Paris, 98 bis boulevard Arago, F-75014 Paris, France
[6] NASA Ames Research Center, Moffett Field, California, USA
[7] Observatoire de l'Université de Genève, 51 chemim des Maillettes, 1290 Sauverny, Switzerland
[8] DTU Space, National Space Institute, Technical University of Denmark, Elektrovej 328, DK-2800 Kgs. Lyngby, Denmark
[9] Department of Astronomy, University of Maryland, College Park, MD, USA
[10] Kavli Institute for Astrophysics and Space Research, Massachusetts Institute of Technology, 77 Massachusetts Avenue, 37-241, Cambridge, MA 02139, USA
[11] NASA Jet Propulsion Laboratory, 4800 Oak Grove Drive, Pasadena, CA 91109, USA
[12] Department of Astronomy and Carl Sagan Institute, Cornell University, 122 Sciences Drive, Ithaca, NY 14853, USA
[13] Center for Astrophysics—Harvard & Smithsonian, 60 Garden Street, Cambridge, MA 02138, USA
[14] Zentrum für Astronomie und Astrophysik, Technische Universität Berlin, Berlin, Germany
[15] Center of Excellence in Information Systems, Tennessee State University, Nashville, TN 37209, USA
[16] Centro de Astrobiología (CSIC-INTA), E-28692 Villanueva de la Cañada, Madrid, Spain
[17] Physics and Astronomy, Stocker Road, University of Exeter, Exeter EX4 3RF, UK
[18] Space Telescope Science Institute, 3700 San Martin Drive, Baltimore, MD 21218, USA
Received 2019 March 27; revised 2019 June 7; accepted 2019 June 11; published 2019 August 1

Abstract

We present *Hubble Space Telescope* (*HST*) near-ultraviolet (NUV) transits of the hot Jupiter WASP-121b, acquired as part of the PanCET program. Time-series spectra during two transit events were used to measure the transmission spectra between 2280 and 3070 Å at a resolution of 30,000. Using *HST* data from 61 Space Telescope Imaging Spectrograph visits, we show that data from *HST*'s Pointing Control System can be used to decorrelate the instrument systematic errors (jitter decorrelation), which we used to fit the WASP-121b light curves. The NUV spectra show very strong absorption features, with the NUV white light curve found to be larger than the average optical and near-infrared value at 6σ confidence. We identify and spectrally resolve absorption from the Mg II doublet in the planetary exosphere at a 5.9σ confidence level. The Mg II doublet is observed to reach altitudes of $R_{pl}/R_{star} = 0.284 \pm 0.037$ for the 2796 Å line and 0.242 ± 0.0431 for the 2804 Å line, which exceeds the Roche lobe size as viewed in transit geometry ($R_{eqRL}/R_{star} = 0.158$). We also detect and resolve strong features of the Fe II UV1 and UV2 multiplets, and observe the lines reaching altitudes of $R_{pl}/R_{star} \approx 0.3$. At these high altitudes, the atmospheric Mg II and Fe II gas is not gravitationally bound to the planet, and these ionized species may be hydrodynamically escaping or could be magnetically confined. Refractory Mg and Fe atoms at high altitudes also indicate that these species are not trapped into condensate clouds at depth, which places constraints on the deep interior temperature.

Key words: planets and satellites: atmospheres – stars: individual (WASP-121) – techniques: photometric – techniques: spectroscopic

1. Introduction

Close-in exoplanets are exposed to immense stellar X-ray and extreme-ultraviolet (UV) radiation. These photons ionize atmospheric species and deposit enormous heat through electron collisions, which can greatly expand the upper atmosphere and drive hydrodynamic outflow and mass escape (Yelle 2004; García Muñoz 2007; Murray-Clay et al. 2009; Owen & Jackson 2012). UV observations of transiting exoplanets are sensitive to these uppermost microbar atmospheric layers, where atomic and ionized species can be detected. Thus far, these detections include species such as H I in Lyα, as well as O I, C II in the far-UV (FUV) and Mg I in the near-UV (NUV; 2000–3000 Å). In the case of HD 209458b, ∼10% UV transit depths were found, indicating an

extended H I, O I, C II, and Mg I exosphere (Vidal-Madjar et al. 2003, 2004, 2013; Ben-Jaffel 2007, 2008; Linsky et al. 2010; Ballester & Ben-Jaffel 2015). Detections of H I and O I have also been made in HD 189733b (Lecavelier des Etangs et al. 2010, 2012; Ben-Jaffel & Ballester 2013). Some of the best examples of escaping exoplanet atmospheres occur in warm-Neptune-mass planets. For GJ 436b (Ehrenreich et al. 2015), an extensive H I atmosphere has been detected, including an extended cometary-like tail. The transit depth reaches ∼50% at Lyα, showing H I extending well beyond the Roche lobe and surviving photo-ionization (Ehrenreich et al. 2015; Lavie et al. 2017). Similarly, the warm Neptune GJ 3470b also shows an extended upper atmosphere of H I (Bourrier et al. 2018), with transit absorption depths reaching 35%.

The most highly irradiated hot Jupiters are expected to have vigorous atmospheric escape. These exoplanets could be excellent probes of evaporation and photoionization, as metals such as Fe and Mg are not condensed into clouds (Visscher et al. 2010; Wakeford et al. 2017), which would otherwise trap these atomic species in the lower atmosphere. Neutral and ionized Fe and Ti have been detected in the ultra-hot Jupiter KELT-9b (Gaudi et al. 2017) from high spectral resolution ground-based observations (Hoeijmakers et al. 2018) as have Mg I and H I in Hα (Yan & Henning 2018; Cauley et al. 2019; Hoeijmakers et al. 2019). As ultra-hot Jupiters are rare and often located in systems far from the Sun, the currently known population is inaccessible to FUV observations due to the prohibitively large absorption by the interstellar medium (ISM). However, these very hot exoplanets are accessible in the NUV where there are numerous atomic spectral lines and the ISM does not pose such a large problem. For the ultra-hot Jupiter WASP-12b, which has an equilibrium temperature of 2580 K, NUV spectrophotometry with the Cosmic Origins Spectrograph (COS) revealed strong broadband absorption signatures between 2539 and 2811 Å. These signatures have been interpreted as a continuum of metal lines absorbing the entire NUV region (Fossati et al. 2010, 2013; Haswell et al. 2012), and excess transit depths were seen at Mg II and Fe II wavelengths. Possible early ingress signatures in Hα and Na have also been seen at optical wavelengths (Jensen et al. 2018). An early ingress was also found which could be a signature of material overflowing the Roche lobe at the L1 Lagrangian point or a magnetospheric bow shock (Lai et al. 2010; Vidotto et al. 2010; Llama et al. 2011; Bisikalo et al. 2013). However, Mg II and Fe II do not exist in the stellar wind or corona, which poses problems for the bow-shock interpretation (Ben-Jaffel & Ballester 2014). These observations were followed up by additional WASP-12b COS observations (Nichols et al. 2015), which also showed significant NUV absorption but did not find evidence for the previously claimed early ingress (see also Turner et al. 2016).

WASP-121b is an ultra-hot Jupiter discovered by Delrez et al. (2016), with a dayside equilibrium temperature above 2400 K. The planet has a mass of $1.18 \pm 0.06\ M_J$, a large inflated radius of $\sim 1.7\ R_J$, and is in a short orbital period around a bright ($V_{mag} = 10.5$) F6V star. WASP-121b is extremely favorable to atmospheric measurements. The planet's dayside emission spectra has been measured in the near-infrared with the *Hubble Space Telescope* (*HST*) Wide Field Camera 3 (WFC3), where a stratosphere has been found exhibiting spectroscopically resolved emission features of H_2O (Evans et al. 2017). The transmission spectra acquired with the *HST* Space Telescope Imaging Spectrograph (STIS) and WFC3 revealed molecular absorption due to H_2O and likely VO (Evans et al. 2016, 2018). In addition, strong NUV absorption signatures between 3000 and 4500 Å were found in the STIS G430L transmission data, which Evans et al. (2018) interpreted as a possible SH signature or some other absorber. NUV observations of WASP-121b have also been made with the SWIFT telescope (Salz et al. 2019), where a tentative excess absorption signature has also been seen.

Here we present *HST* transmission spectrum results for WASP-121b from the Panchromatic Exoplanet Treasury (PanCET) program (*HST* GO-14767; P.I.s Sing & López-Morales), which consists of multi-wavelength transit and eclipse observations for 20 exoplanets. In this work, we present new

HST NUV transit observations with the Space Telescope Imaging Spectrograph (STIS). We describe a new method to decorrelate time series *HST* light curves in Section 2, present our observations in Section 3, give the analysis of the transit light curves in Section 4, discuss the results in Section 5, and conclude in Section 6.

2. Hubble Jitter Decorrelation

HST spectrophometric light curves taken with the STIS show instrument-related systematic effects that are widely thought to be caused by the thermal breathing of the *HST*. The thermal breathing trends cause the point-spread function (PSF) to change repeatedly for each 90 minute spacecraft orbit around the Earth, producing corresponding photometric changes in the light curve (Brown et al. 2001). These systematic trends have widely been removed by a parameterized deterministic model, where the photometric trends are found to correlate with a number n of external detrending parameters (or optical state parameters, x). These parameters describe changes in the instrument or other external factors as a function of time during the observations, and are fit with a coefficient for each optical state parameter, p_n, to model and detrend the photometric light curves. In the case of *HST* STIS data, external detrending parameters including the 96 minute *HST* orbital phase, ϕ_{HST}, the X_{psf} and Y_{psf} detector position of the PSF, and the wavelength shift S_λ of the spectra have been identified as optical state parameters (Brown et al. 2001; Sing et al. 2011). This set of detrending parameters (hereafter called the "traditional model") has been widely used to fit *HST* transit and eclipse light curves (e.g., Huitson et al. 2013; Wakeford et al. 2013; Nikolov et al. 2014; Demory et al. 2015; Sing et al. 2016; Lothringer et al. 2018), and even non-parametric models like Gaussian processes still rely on these detrending parameters of the traditional model as inputs (Bell et al. 2017; Gibson et al. 2017). In addition to the STIS CCD with the G430L, G750L, and G750M STIS gratings, these detrending parameters have been used to fit STIS Echelle E230M data, which use the Multi-Anode Microchannel Array (NUV-MAMA) detector.

A potential source of astrophysical noise from our main-sequence FGK target stars is expected to be photometric variations due to stellar activity, with star spots modulating the total brightness of the star in a quasi-periodic fashion on timescales similar to the rotation period of the star (typically ranging from a few days to a few weeks). However, our *HST* transit observations only span 6.4–8 hr (four or five *HST* orbits), which is short compared to the stellar rotational period. The small fraction of the stellar rotation period observed strongly limits the photometric amplitude of any rotational modulation in our transit light curves, and makes any quasi-periodic variations appear as linear changes in the baseline stellar flux. We estimate that highly active stars variable at the 1% level in the optical over 10 day periods (similar to HD 189733A) would be expected to have photometric stellar activity change the baseline stellar flux during the *HST* visit by ~600 ppm or less. Inactive stars such as WASP-12A, which is photometrically quiet below 0.19% (Sing et al. 2013), would be expected to have an upper limit to a stellar activity signal of 100 ppm during our transit observations, which is below the photon noise limit of a typical STIS CCD white-light-curve exposure. These potential astrophysical noise sources can be

modeled by fitting a linear function of time to the transit light curves, ϕ_t.

There are still limitations with the traditional model in detrending instrument-related systematic effects. Notably, the first orbit in *HST* STIS visits has generally been discarded as it takes one spacecraft orbit for the telescope to thermally relax, which compromises the photometric stability of the first orbit of each *HST* visit beyond the limits of the traditional model. To help reduce the level of systematic errors in *HST* STIS measurements, in this paper we investigated additional optical state parameters which could be used to help decorrelate transit or eclipse light curves. Rather than attributing all the trends to a thermal breathing effect, we explored parameters under the assumption that the stability of the telescope pointing itself (and subsequent effects such as slit light losses) is a limiting factor. The jitter files are products of the Engineering Data Processing System (EDPS), which describes the performance of *HST*'s Pointing Control System during the duration of an observation.[19] The files contain a determination of the telescope pointing during an observation utilizing Fine Guidance Sensor guidestar measurements to map the telescope's focal plane onto an R.A. and decl. The determination is accurate to the level of the guidestar positional uncertainty and the knowledge of the telescope's focal plane geometry, which is typically at the sub-pixel level. The data contained in the jitter files are time-tagged and recorded in 3 s averages, thus providing suitable fidelity to describe the pointing during transiting exoplanet observations, which have science frame exposure times typically of several minutes.

For an *HST* visit, we extracted the time-tagged engineering information from the jitter files (extension_*jit.fits*) for each science exposure by taking the median value of each measured quantity between the beginning and end date of the exposure. We found that using the median made the values less sensitive to occasional bad values recorded in the jitter files (a known issue). For the jitter file measurement of the *HST* sub-point longitude, measured in degrees between 0 and 360, care was taken to prevent a value discontinuity in the time series at 360°. For use in decorrelation as optical state vectors, we then normalized each measured quantity by removing the mean value from each variable and then dividing the values by the standard deviation (see the Appendix for additional details).

2.1. Global STIS Light Curve–Jitter Correlation Trends

The jitter files include 28 different engineering measurements (see Table 1). To determine the suitability of each of the jitter optical state vectors for decorrelating transit or eclipse light curves, we measured the linear Pearson correlation coefficient, R, between each jitter vector and the out-of-transit white-light-curve photometric data for 61 separate *HST* visits covering close to 300 spacecraft orbits. Specifically, we used all of the STIS G430L and G750L data from 23 visits of program GO-12473 (P.I. Sing), G430L, and G750L data from 34 visits of GO-14767 (P.I.s Sing & López-Morales), and four G430L visits from GO-14797 (P.I. Crossfield). The data from each *HST* STIS visit were reduced in the same manner as detailed in Sing et al. (2016), and we summed the counts of each extracted spectra to produce a white-light curve for each visit. Using the out-of-transit data, the percent of variance in common between jitter decorrelation parameters and the STIS

Table 1
Jitter Engineering Data Optical State Vectors (Column 1) and the Correlation R^2 Values (in %) with the White Light Curve Photometry for the Visits Covering a STIS/G430L Eclipse of WASP-12 (Column 1) and the STIS/E230M Data of WASP-121 for Visits 97 and Visit 98 (Columns 3 and 4, Respectively)

Vector (1)	W-12 (2)	W-121 (3)	W-121 (4)	$\overline{R^2}$ (5)	$\sigma_{\overline{R^2}}$ (6)
ϕ_{HST}	36	54	17	34	28
S_λ	86	0	2	30	27
X_{psf}	26	30	1	19	22
Y_{psf}	31	30	1	16	20
V2_dom	16	13	6	7	9
V3_dom	1	1	0	6	8
V2_roll	57	36	7	36	29
V3_roll	54	34	9	35	29
SI_V2_AVE	0	11	19	4	5
SI_V2_RMS	56	8	0	19	20
SI_V2_P2P	58	15	0	19	20
SI_V3_AVE	4	14	15	5	6
SI_V3_RMS	55	29	6	12	15
SI_V3_P2P	55	5	2	13	15
R.A.	55	37	8	31	28
Decl.	57	36	7	29	27
Roll	56	50	13	14	16
LimbAng	8	0	3	10	14
TermAng	0	7	3	8	9
LOS_Zenith	8	0	3	10	14
Lat	13	41	7	20	21
Long	76	6	0	38	29
Mag_V1	1	22	8	13	15
Mag_V2	12	4	0	16	19
Mag_V3	12	29	4	15	16

Note. The average R^2 value from 61 *HST* STIS G430L & G750L CCD visits, $\overline{R^2}$, is also reported in column 5, and the standard deviation of R^2 in column 6.

white-light-curve photometry, R^2, was determined for each of the 61 visits. We also measured the quantity for the traditional detrending variables (ϕ_{HST}, X_{psf}, Y_{psf}, and S_λ) with the results given in Table 1. As a point of comparison, the individual R^2 values for a G430L eclipse of WASP-12b are reported in addition to the two STIS E230M transits of WASP-121b which are visits 97 and 98 of the PanCET program. The raw white-light curve of the STIS G430L eclipse of WASP-12b reaches a photometric precision of 979 ppm, as measured by the standard deviation of the light curve about the mean, which is a factor of $6.4\times$ higher than expected from the photon noise levels.

An additional systematic trend is seen in the STIS CCD time-series data, where the first exposure of each spacecraft orbit is consistently found to exhibit significantly lower fluxes than the remaining exposures (Brown et al. 2001; Sing et al. 2011). Attempts were made to mitigate this effect in the observational setup by employing a quick 1 s integration (Sing et al. 2015), which was discarded. However, higher overall correlation values were found between the STIS CCD white-light curves and the optical state vectors if, in addition, the first long science exposure of every orbit was also systematically discarded from the analysis. We suspect the 1 s integration technique is not an overall effective method to mitigate the first-orbit-exposure systematic, and the first long science exposure of any STIS CCD orbit in a time-series analysis should be treated with caution. For the correlation analysis and for all subsequent CCD light curve fitting throughout this

---
[19] See http://www.stsci.edu/hst/observatory/pointing/ for additional details.

Table 2
WASP-121b Broadband Transmission Spectral Results and Nonlinear Limb Darkening Coefficients for the STIS E230M

λ_c (Å)	$\Delta\lambda$ (Å)	R_P/R_*	σ_{R_P/R_*}	c_1	c_2	c_3	c_4
2673	799	0.13735	0.00257	0.4011	−0.2625	1.2818	−0.4674
2387	236	0.15300	0.00845	0.4282	−0.8777	1.6772	−0.2513
2600	200	0.13962	0.00465	0.4826	−0.6976	1.9529	−0.7708
2800	200	0.13760	0.00366	0.4090	−0.2445	1.1797	−0.3940
2986	172	0.12734	0.00389	0.3374	0.2045	0.8312	−0.4348

paper, we chose to discard the first long science exposure of each *HST* orbit.

From the correlation analysis, we identify several pairs of jitter vectors that are often found to correlate well with the STIS data ($R^2 \gtrsim 30\%$, also see the Appendix). The roll of the telescope along the V2 and V3 axis (*V2_roll*, *V3_roll*) and the R.A. and decl. of the aperture reference *R.A.* and *decl.* are two pairs of vectors that are both related to the pointing of the telescope and in some data sets are found to highly correlate with the data with R^2 values as high as 90%. In addition, the *HST* sub-point latitude and longitude (*Lat* and *Long* respectively) are seen to have large correlations. The latitude and longitude are similar in nature (but not identical) to ϕ_{HST}, which is already included in the traditional model. From *HST* visit to visit, the correlation values themselves for any particular vector are found to change by large amounts, which is reflected in Table 1 by the large standard deviation values, σ_{R^2}. However, in retrospect a large spread in correlation values related to the telescope's position is to be expected. Different targets across the sky observed at different telescope orientation values will not necessarily favor any particular telescope axis or *R.A.* and *decl.* direction, but rather the actual vector direction(s) the target PSF takes with respect to the instrument during a transit observation. We note a general trend where the R^2 values in visits with relatively good pointing show lower levels of correlation (e.g., visit 98), while visits with poorer quality pointing show higher levels of correlation (e.g., visit 97).

Trends with telescope position are consistent with photometric systematics caused by slit light losses. If correct, the trends appear even when using slit sizes that are much greater than the size of the PSF. Our hypothesis is that the known telescope breathing leads to small changes in the position of the PSF on the detector (usually at the sub-pixel level), which largely manifest themselves as slit light losses. Even if the central PSF is well centered on a much wider slit, diffraction spikes and the wide wings of the PSF could contribute to light losses. If the dominant sources of systematics with STIS are position-related slit light losses, assuming similar guiding performance, then presumably there could be larger systematics when using small slits such as the 0″.2 × 0″.2 used with the STIS E230M compared to the 52″ × 2″ slit used with the CCD. In addition, there would be larger systematics in visits with poorer guiding performance, which appears to be the case. Several STIS visits in the PanCET program had guide star acquisition problems, which resulted in reduced pointing accuracy and light curves with comparably larger systematic trends. We also observe that the jitter vectors (*V2_roll*, *V3_roll*) and (*R.A.*, *decl.*) often have the same general trends as the traditional vectors (S_λ, X_{psf}, and Y_{psf}), which are measured directly from the spectra. Similar trends are generally expected,

as changes in the PSF position (measured through the telescope position in the jitter files) will also be recorded by changes in the placement of the target stellar spectra on the detector. These vectors are not identical, however, as the detector-measured vectors will also be sensitive to further detector effects such as the pixel-to-pixel flat-fielding, while the jitter vectors are able to record the telescope position regardless of whether the target PSF is contained within the slit.

As a test, we implemented jitter detrending on the STIS G430L eclipse data of WASP-12b, finding good agreement in the eclipse depth with Bell et al. (2017) who used a Gaussian process method to decorrelate the time series data (see the Appendix). However, several improvements can be seen utilizing jitter detrending. The best-fit measured eclipse depth was found to be positive while Bell et al. (2017) found a negative value. In addition, with jitter detrending the first orbit was successfully recovered for use in the analysis, while Bell et al. (2017) had to discard it.

3. Observations

3.1. HST STIS NUV Spectroscopy

We observed two transits of WASP-121b with the *HST* STIS E230M echelle grating during 2017 February 23 (visit 97) and 2017 April 10 (visit 98). The observations were conducted with the NUV-MAMA detector using the Echelle E230M STIS grating and a square 0″.2 × 0″.2 entrance aperture. The E230M spectra had resolving power of $\lambda/(2\Delta\lambda) = 30{,}000$ and was configured to the 2707 Å setting to cover the wavelength ranges between 2280 and 3070 Å in 23 orders (see Figure 1). The resulting spectra had a dispersion on the detector of approximately 0.049 Å/pixel. Both transits covered five *HST* spacecraft orbits, with the transit event occurring in the third and fourth orbits. During each *HST* orbit, the spectra were obtained in TIME-TAG mode, where the position and detection time of every photon was recorded in an event list, which had 125 μs precision.

We sub-divided the spectrum of each *HST* spacecraft orbit into sub-exposures with the Pyraf task inttag, each with a duration of 274.01996 s. This allowed orbits 2 through 5 to be divided into 10 sub-exposures each, while the first orbit was divided into seven sub-exposures. These sub-exposures were then each reduced with CALSTIS version 3.17, which includes the calibration steps of localization of the orders, optimal order extraction, wavelength calibration, and flat-field corrections. The mid-time of each exposure was converted into barycentric Julian dates in barycentric dynamical time (BJD$_{TBD}$) for use in the transit light curves (Eastman et al. 2010).
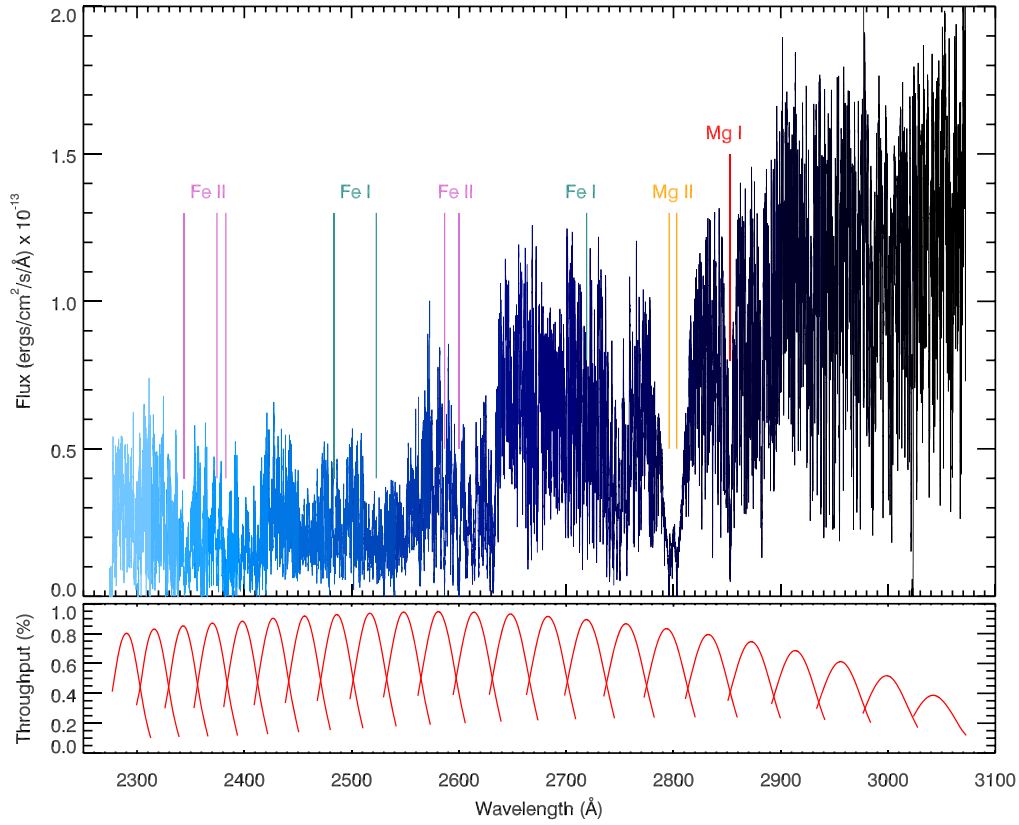
Figure 1. Top: flux-calibrated out-of-transit spectrum of WASP-121A; each order is plotted in a different color. Several resonant lines of Mg and Fe are indicated. Bottom: the instrumental throughput of each order.

4. Analysis

4.1. STIS E230M Light-curve Fits

The light curves were modeled using the analytical transit models of Mandel & Agol (2002). For the white-light curves, the central transit time, planet-to-star radius ratio, stellar baseline flux, and instrument systematic trends were fit simultaneously, with flat priors assumed. The inclination and stellar density (or equivalently the semimajor axis to stellar radius ratio, a/R_{star}) were held fixed to the values found in Evans et al. (2018), as fitting for these parameters found values consistent with the literature, though with an order of magnitude lower precision. For example, we find a value of $a/R_{star} = 3.63 \pm 0.16$ from the NUV white-light curve of visit 98, while Evans et al. (2018) reports a value of 3.86 ± 0.02. Compared to the NUV data here, the study of Evans et al. (2018) benefits from much higher photometric precision in a larger data set with a wider array of wavelengths, including STIS data with complete phase coverage of the transit, which constrains the planet's orbital system parameters to a much greater degree than the NUV data alone.

The total parameterized model of the flux measurements over time, $f(t)$, was modeled as a combination of the theoretical transit model, $T(t, \theta)$ (which depends upon the transit parameters θ), the total baseline flux detected from the star, F_0, and the instrument systematics model $S(x)$, giving

$$f(t) = T(t, \theta) \times F_0 \times S(x). \quad (1)$$

Based on the results of Section 2 and the Appendix, for our most complex systematics error model tested, we included a linear baseline time trend, ϕ_t, as well as the traditional optical

state vectors (ϕ_t, ϕ_{HST}, ϕ_{HST}^2, ϕ_{HST}^3, ϕ_{HST}^4, X_{psf}, Y_{psf} and S_λ) and jitter vectors (*V2_roll*, *V3_roll*, *R.A.*, *decl.*, *Lat*, and *Long*) resulting in up to 14 terms used to describe $S(x)$ depending on the data set in question as described below.

The errors on each data point were initially set to the pipeline values, which are dominated by photon noise. The best-fitting parameters were determined simultaneously with a Levenberg–Marquardt (L-M) least-squares algorithm (Markwardt 2009) using the unbinned data. After the initial fits, the uncertainties for each data point were rescaled to match the standard deviation of the residuals. A further scaling was also applied to account for any measured systematic errors correlated in time ("red noise"). After rescaling the error bars, the light curves were then refit, thus taking into account any underestimated errors in the data points.

The red noise was measured by checking whether the binned residuals followed an $N^{-1/2}$ relation, when binning in time by N points. In the presence of red noise, the variance can be modeled to follow a $\sigma^2 = \sigma_w^2/N + \sigma_r^2$ relation, where σ_w is the uncorrelated white noise component, and σ_r characterizes the red noise (Pont et al. 2006). For our best-fitting models for $S(x)$, we did not find evidence for substantial red noise.

The uncertainties on the fitted parameters were calculated using the covariance matrix from the Levenberg–Marquardt algorithm, which assumes that the probability space around the best-fit solution is well-described by a multivariate Gaussian distribution. Previous analyses of other *HST* transit observations (Berta et al. 2012; Line et al. 2013a; Sing et al. 2013; Nikolov et al. 2014) have found this to be a good approximation when fitting *HST* STIS data. We also computed uncertainties with a Markov chain Monte Carlo (MCMC)

analysis (Eastman et al. 2013), which does not assume any functional form for this probability distribution. In each case, we found equivalent results between the MCMC and the Levenberg–Marquardt algorithm for both the fitted parameters and their uncertainties, as the posterior distributions were found to be Gaussian. Inspection of the 2D probability distributions from both methods indicates that there are no significant correlations between the systematic trend parameters and the planet-to-star radius contrast.

4.2. Limb Darkening

The effects of stellar limb darkening are strong at NUV wavelengths. To account for the effects of limb darkening on the NUV transit light curve, we adopted the four-parameter, nonlinear limb-darkening law, calculating the coefficients as described in Sing (2010). For the model, we used the 3D stellar model from the Stagger-grid (Magic et al. 2015) with the model ($T_{eff} = 6500$, $\log g = 4$, [Fe/H] = 0.0), which was closest to the measured values of WASP-121A in effective temperature, gravity, and metallicity ($T_{eff} = 6460 \pm 140$ K, $\log 10 \ g = 4.242 \pm 0.2$ cgs, [Fe/H] = +0.13 $\pm$ 0.09 dex; Delrez et al. 2016). The Stagger-grid 3D models are calculated at a resolution of $R = 20{,}000$ which is close to the native resolution of the E230M data ($R = 30{,}000$), and contains a fully line-blanketed NUV region that matches the flux-calibrated data of WASP-121A well (see Figure 2). We included the individual responses from each order in the echelle spectra and converted the stellar model spectral wavelengths from air to vacuum. We also applied a wavelength shift to the data to take into account the systemic radial velocity of the system, 38.36 km s^{-1} (Gaia Collaboration et al. 2018), shifting the star to the rest frame.

In a test to see how well the 3D models performed, we fit visit 98 with a three-parameter limb-darkening law (see Sing 2010) and let the linear coefficient, c_2, fit freely while the other two nonlinear parameters were fixed to the model values. We found good agreement at the 1σ level between the fit coefficient $c_2 = 0.881 \pm 0.215$ and the theoretical value of 1.077. In addition, the fit $R_{pl}/R_{star} = 0.1415 \pm 0.0050$ was also consistent (within 1σ) when fitting for c_2 versus fixing the limb darkening (see Section 4.4). For the remainder of the study, we fixed the limb-darkening coefficients to the model values. We note that using the second-order Akaike information criterion (AICc) for model selection (see the Appendix), that the AICc favored fixing the limb-darkening parameters to the model values.

4.3. Updated Ephemeris with Transiting Exoplanet Survey Satellite Data

The Transiting Exoplanet Survey Satellite (TESS) observed WASP-121b in camera 3 from 2019 January 7 to 2019 February 2, and we obtained the time-series photometry though the Mikulski Archive for Space Telescopes' exo.MAST[20] web service. We fit the TESS WASP-121b transits using the Presearch Data Conditioning light curve, which has been corrected for effects such as non-astrophysical variability and crowding (Stumpe et al. 2012; Jenkins et al. 2016). From the time series, we removed all of the points that were flagged with anomalies. The time-series barycentric TESS Julian dates were converted to BJD$_{TDB}$ by adding 2,457,000 days. The TESS light curve
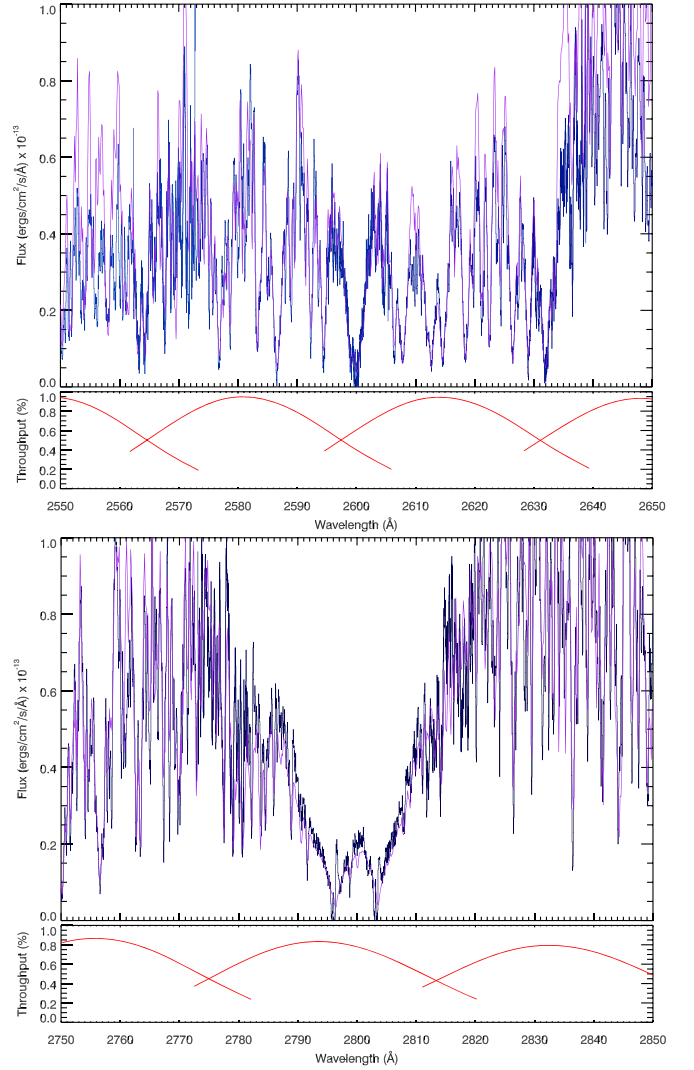
---

20 https://exo.mast.stsci.edu

Figure 2. Same as Figure 1, but zoomed in on two wavelength regions covering an Fe II line at 2600 Å and the Mg II doublet at 2796.35 and 2803.53 Å with the 3D Stagger-grid model overplotted (purple).

contains data for 16 complete transits of WASP-121b and one partial transit. For each transit in the light curve, we extracted a 0.5 day window centered around the transits and fit each transit event individually. We fit the data using the model as described in Sections 4.1 and 4.2, though only included a linear baseline time trend, ϕ_t, for $S(\boldsymbol{x})$. We found a weighted-average value of $R_{pl}(TESS)/R_{star} = 0.12342 \pm 0.00015$, which is in good agreement with the HST transmission spectrum of Evans et al. (2018). We converted the transit times of Evans et al. (2018) and (Delrez et al. 2016) to BJD$_{TDB}$ using the tools from Eastman et al. (2010) and fit these along with the TESS transit times and visit 98 from Section 4.4 with a linear function of the period P and transit epoch E:

$$T(E) = T_0 + EP. \qquad (2)$$

We find a period of $P = 1.2749247646 \pm 0.0000000714$ (days) and central transit time of $T_0 = 2457599.551478 \pm 0.000049$ (BJD$_{TDB}$). We find a very good fit with a linear ephemeris (see Figure 3), having a χ^2 value of 16.8 for 21 degrees of freedom (dof). We find no obvious signatures of quasi-periodic
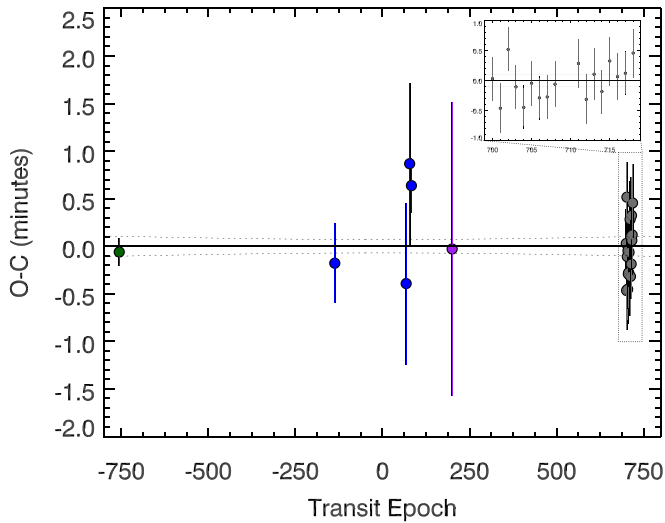
Figure 3. Observed–calculated mid-transit times of WASP-121b. Included are the results from Delrez et al. (2016) (dark green) and Evans et al. (2018) (blue) as well as the the NUV transit time (purple) and *TESS* times (gray) from this work. A zoom-in around the *TESS* mid-transit times is also shown. The 1σ error envelope on the ephemeris is plotted as the horizontal dashed lines.

photometric variabiltiy due to stellar activity, with the *TESS* data binned by 62 minutes (excluding the transit and eclipse times) giving a standard deviation about the mean of 0.07%, which is only modestly higher than the expected photometric precision of 0.02%.

4.4. White-light-curve Fits

Visits 97 and 98 show dramatically different levels of instrumental systematic trends (see Figure 4). In particular, visit 97 shows a ∼4% change in flux in the fifth out-of-transit orbit, while for visit 98 there is no such large trend, and the light curve points are within ∼0.4% of each other. Upon inspection of the telescope *R.A.* and *decl.* from the jitter files, it is clear that visit 97 suffers from a very large drift during the five orbits covering the transit event, while visit 98 has much more stable pointing (see Figure 5). The large drift likely leads to large slit light losses in visit 97. Most importantly, the *R.A.* and *decl.* positions of the telescope during the transit in visit 97 are significantly different from the out-of-transit positions, especially the fifth orbit, which was shifted by about a quarter of a pixel. As discussed in Gibson et al. (2011), detrending with optical state vectors can only be expected to work if we interpolate the vectors for the in-transit orbit(s) with the out-of-transit orbits, which requires the baseline function to be well represented by the linear model over the range of the decorrelation parameters.

For each visit, we used the AICc and measured σ_r to determine the optimal optical state vectors to include from the full set without overfitting the data while minimizing the red noise. As found in Section 2, the different position-related vectors from the jitter files typically contained similar trends. For visit 98, we found it was optimal to include ϕ_{HST} terms up to second order, as well as the jitter detrending vectors *V2_roll*, *V3_roll*, and *R.A.* We rotated the roll vector pair (*V2_roll*, *V3_roll*), which are contained in the engineering jitter files relative to the axis of the square slit (*Vn_roll*, *Vt_roll*), which is rotated by about 45° relative to the spacecraft orientation

reference vector U3, such that $S(\boldsymbol{x})$ could be written as

$$S(\boldsymbol{x}) = p_1\phi_t + p_2\phi_{HST} + p_3\phi_{HST}^2 \\ + p_4\mathrm{R.A.} + p_5 Vn_{\mathrm{roll}} + p_6 Vt_{\mathrm{roll}} + 1. \qquad (3)$$

The fit values of interest, namely $R_{\mathrm{pl}}/R_{\mathrm{star}}$, did not substantially change for any of the top fitting models (AICc–AICc$_{\mathrm{min}} \lesssim 6$). With nine free parameters ($R_{\mathrm{pl}}/R_{\mathrm{star}}$, F_0, T_0, $p_{1..6}$), the fit achieves a signal-to-noise which is 81% of the theoretical photon noise limit, with no detectable red noise and a χ^2_ν of 1.21 for 37 dof. We note that including the jitter corrections and the second-order breathing polynomial not only provides a significantly better fit than the traditional systematics model, but we were also able to make use of the first orbit in the visit. The overall photometric performance is similar to that achieved with the STIS CCD using the G430L or G750L, despite the use of a much narrower slit. With visit 97, we measure the white-light curve $R_{\mathrm{pl}}/R_{\mathrm{star}} = 0.1374 \pm 0.0026$ (see Table 2) and a $T_0 = 2457854.536411 \pm 0.001073$ (BJD$_{\mathrm{TBD}}$). The central transit time agrees very well with the expected ephemeris, occurring -0.2 ± 1.6 min relative to the expected central transit time using the updated ephemeris from Section 4.3.

For visit 97, even the most complex model did not achieve fit residuals as small as visit 98. As noted above, the fifth orbit of the visit displays dramatically increased systematic trends compared to the other orbits, with the position of the telescope during the orbit being relatively far from the position of the in-transit orbits (see Figure 5). As such, we find $R_{\mathrm{pl}}/R_{\mathrm{star}}$ can change dramatically (by about 0.016 $R_{\mathrm{pl}}/R_{\mathrm{star}}$) between differing systematics models when including the data from the fifth orbit in the light-curve fits. Given these factors, we find that it is preferable to drop the last orbit from the analysis when measuring the absolute transit depths in visit 97. This is similar to many *HST* STIS and WFC3 transit studies that have dropped the first orbit as it usually displays larger non-repeatable trends due to changes in the thermal breathing or charge trapping. When excluding the fifth orbit, we found the fit $R_{\mathrm{pl}}/R_{\mathrm{star}}$ values did not change substantially between differing systematics models (∼0.008 $R_{\mathrm{pl}}/R_{\mathrm{star}}$), and using the AICc, we found $S(\boldsymbol{x}) = S(RA, Vn_{\mathrm{roll}}, Vt_{\mathrm{roll}}, \phi_t)$ to be optimal. The best-fit planet radius for visit 97 was found to be $R_{\mathrm{pl}}/R_{\mathrm{star}} = 0.1364 \pm 0.0110$, which matches the value from visit 98 at well within 1σ, and achieves 43% of the theoretical photon noise limit.

4.5. Spectroscopic Fits

When measuring the transmission spectrum, $R_{\mathrm{pl}}(\lambda)/R_{\mathrm{star}}$, we fixed the system parameters as they are not expected to have a wavelength dependence. In addition, we fixed the the limb-darkening coefficients to those determined from the stellar model for each spectroscopic passband, using the same method as described in Section 4.2. The light-curve-fitting methods were otherwise identical to those described in Section 4.1. We fit each spectroscopic light curve with the same functional systematics model as was found to optimally fit the white-light curve, fitting the various spectroscopic bins simultaneously for the wavelength-dependent $R_{\mathrm{pl}}(\lambda)/R_{\mathrm{star}}$ and systematic parameters $p_{1..6}$.

Figure 6 shows our resulting broadband spectra from visit 98 in ∼200 Å bins, as well as the NUV white-light-curve value. $R_{\mathrm{pl}}(\lambda)/R_{\mathrm{star}}$ is observed to sharply rise toward shorter wavelengths. The overall NUV transmission spectrum shows strong
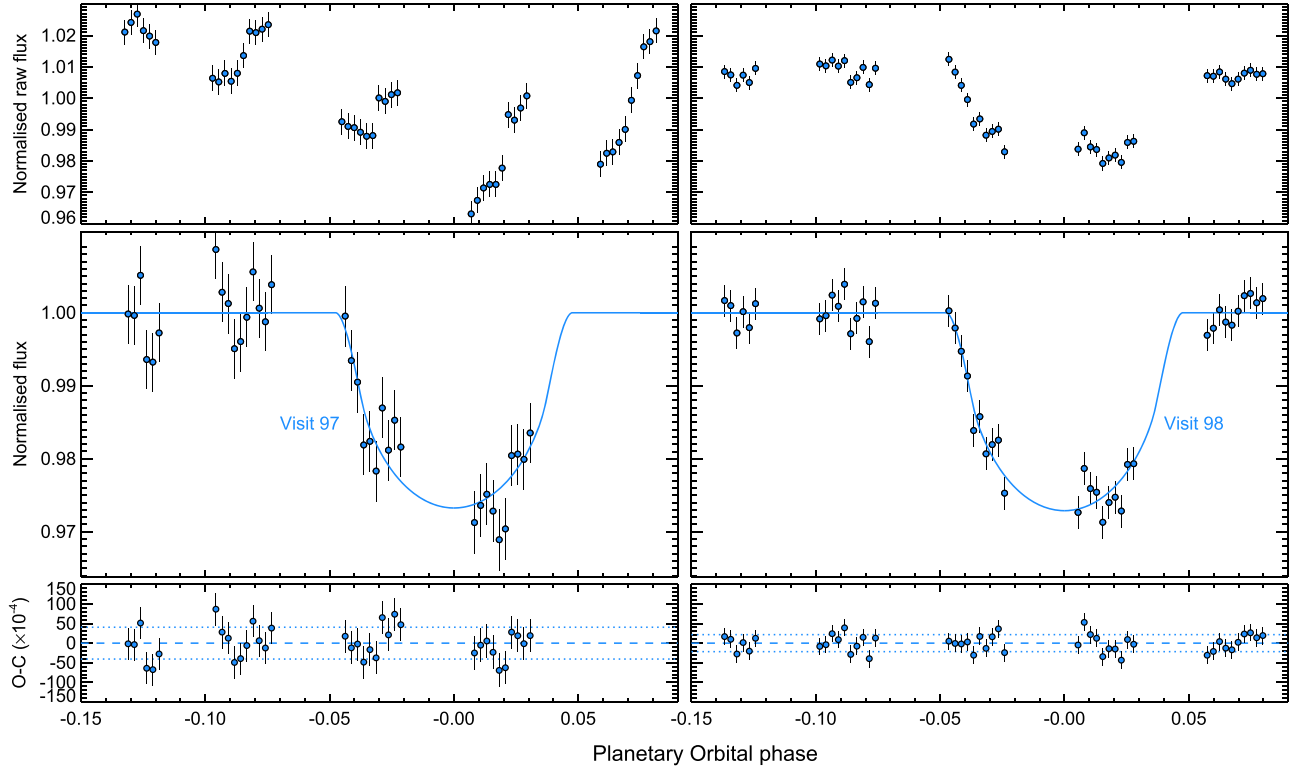
Figure 4. WASP-121b E320M white-light curves for visits 97 (left) and 98 (right). The top plot contains the raw flux, the middle panels contain the flux with the fitted instrument systematics model removed, and the bottom panel shows the residuals between the data and the best-fit model.
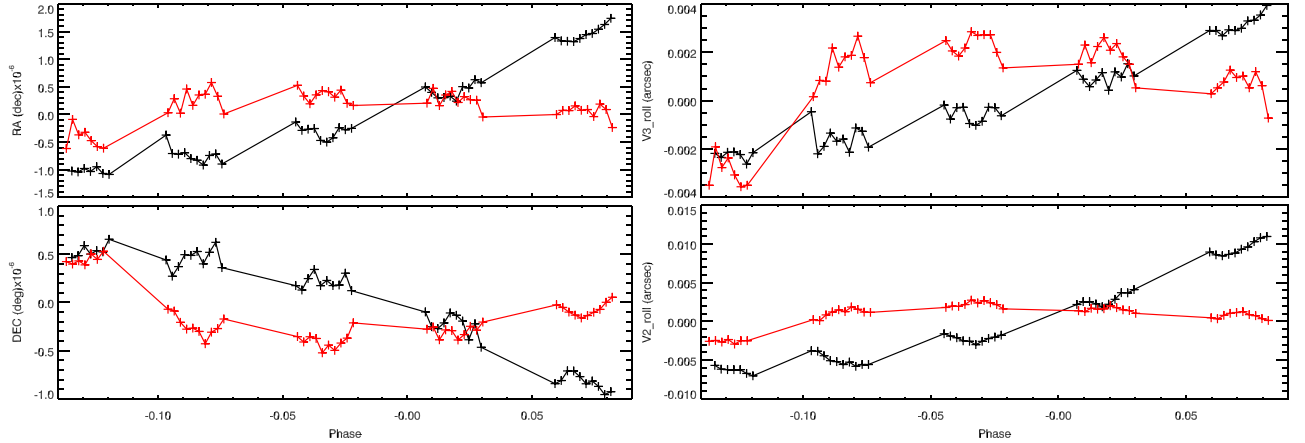

Figure 5. Relative telescope *R.A.*, *decl.*, $V2_{\mathrm{roll}}$, and $V3_{\mathrm{roll}}$ for visit 97 (black) and visit 98 (red).

extinction and is substantially higher than the optical and near-infrared, reaching altitudes of $\Delta R_{\mathrm{pl}}(\lambda)/R_{\mathrm{star}} = 0.0157 \pm 0.0026$ higher in the atmosphere. This is more than $18\times$ the size of the pressure scale height of the lower planetary atmosphere, $H = kT/\mu g$, that is $H/R_{\mathrm{star}} = 0.00084$ at a temperature T of 2000 K.

While the overall transit depths of visit 97 are dependent upon the choice of $S(x)$, the steep rise in the NUV broadband spectrum can be seen regardless of including or excluding the fifth orbit from the analysis. When including the fifth orbit, a systematics model of $S(x) = S(\phi_{HST}, S_\lambda, R.A., decl., Vn_{\mathrm{roll}})$ produces a fit radius that is both consistent with visit 98 and independent of excluding the fifth orbit. The resulting broadband transmission spectrum is shown in Figure 6, which matches well with the results of visit 98.

Given the much lower precision and the sizeable systematic uncertainty of including or excluding the fifth orbit in visit 97, we elect to report the transmission spectra at higher resolutions using visit 98 only. We fit the data to various resolutions and report the transmission spectra at a resolution of $R \sim 650$, corresponding to 4 Å bins with results from 5 Å bins also reported in Section 4.6. At these bin sizes, each light curve point has a few thousand photons and the $\sim 1.5\%$ transit depth can typically be detected across the E230M wavelength range. However, in the spectral regions with strong stellar absorption lines, or at the edges of the spectral orders where the efficiency is low, the transit itself is not always detected due to the lack of flux. At this resolution, strong atomic transitions can be resolved and probed efficiently and resolution-linked bias is

minimized (Deming & Sheppard 2017). Given the high resolution on the E230M, each 4 Å bin still contains ∼60 pixels. To help probe the central wavelength of the observed features more precisely, we also measured the transmission spectra in multiple 4 Å bin sets, each set shifted by 1 Å, corresponding to about $100 \, \mathrm{km \, s^{-1}}$ velocity shifts (see Figure 7). We removed points where the transit was not detected ($R_{\mathrm{pl}}(\lambda)/R_{\mathrm{star}} < 0.05$) or had large errors ($\sigma_{R_P/R_*} > 0.09$), which predominantly occurred within strong stellar lines or at the order edges. The $R \sim 650$ NUV transmission spectra can be seen in Figures 8–11.

4.6. Mg I, Mg II, Fe I, and Fe II

We find no evidence for absorption by Mg I. In a 5 Å band centered on the ground-state Mg I line at 2852.965 Å, we measure a $R_{\mathrm{pl}}(\mathrm{Mg \, I})/R_{\mathrm{star}} = 0.100 \pm 0.056$, which is consistent at the 1σ confidence level with the optical and near-infrared value.

We find strong evidence for absorption by Mg II. We detect and resolve absorption by both the k and h features of the Mg II ground-state doublet located at 2796.35 and 2803.53 Å respectively (see Figure 11). In 5 Å passbands, the transmission spectra in the Mg II doublet are found to have radii of $R_{\mathrm{pl}}(\mathrm{Mg \, II,k})/R_{\mathrm{star}} = 0.284 \pm 0.037$ and $R_{\mathrm{pl}}(\mathrm{Mg \, II,h})/R_{\mathrm{star}} = 0.242 \pm 0.0431$, substantially larger than the values at optical and near-infrared (OIR) wavelengths ($R_{\mathrm{pl}}(\mathrm{OIR})/R_{\mathrm{star}} = 0.1217$) and larger than the average NUV value of $R_{\mathrm{pl}}(\mathrm{NUV})/R_{\mathrm{star}} = 0.1374 \pm 0.0026$. A 10 Å passband split to cover the Mg II doublet simultaneously is found to have a radius value of $R_{\mathrm{pl}}(\mathrm{Mg \, II, h, k})/R_{\mathrm{star}} = 0.271 \pm 0.024$ (see Figure 12), which is 5.4σ above the white-light-curve $R_{\mathrm{pl}}(\mathrm{NUV})/R_{\mathrm{star}}$ value. In the continuum region surrounding the Mg II doublet, no other substantial absorption features are observed and almost all of the spectral bins in a 100 Å region around the doublet are consistent with the $R_{\mathrm{pl}}(\mathrm{OIR})/R_{\mathrm{star}}$ value (see Figure 11).

The strong Mg II absorption can also be seen in the transit light curves, with Figure 12 showing transit depths of about 8% within the Mg line, while the surrounding continuum is consistent with the OIR transit depth of 1.5%. The stellar Mg II double line cores exhibit narrow emission lines, associated with the stellar corona (see Figure 2) with both peaks found just redward of the line centers at velocities near 20–$40 \, \mathrm{km \, s^{-1}}$. We performed several checks to ensure that the presence of the emission line did not adversely affect the planetary Mg II signal. Inspecting the photometric time series of just the stellar Mg II emission lines, we do not observe any substantial variability differences from that of the surrounding continuum. In addition, when scanning the transmission spectrum over the Mg II region, we find the peak of the transmission spectrum is found 50–$100 \, \mathrm{km \, s^{-1}}$ blueward of the Mg II line cores, rather than redward where the emission lines are located.

The transmission spectrum contains a very strong absorption feature at 2381.5 Å ($R_{\mathrm{pl}}(2381.5)/R_{\mathrm{star}} = 0.332 \pm 0.074$), which can be identified as a ground-state resonant transition of Fe II. Fe II transitions occur in a set of multiplets, with notable transitions at 2600, 2382, and 2344 Å for the UV1, UV2, and UV3 multiplets respectively. For the aforementioned UV1 and UV3 ground-state transitions, the stellar line is strong enough such that almost no flux is measured in the line cores (see Figure 2), so the transmission spectrum of the planet cannot be measured with sufficient precision at those wavelengths. However, other candidate Fe II features are also seen in the stellar spectrum (see Figures 8–10).
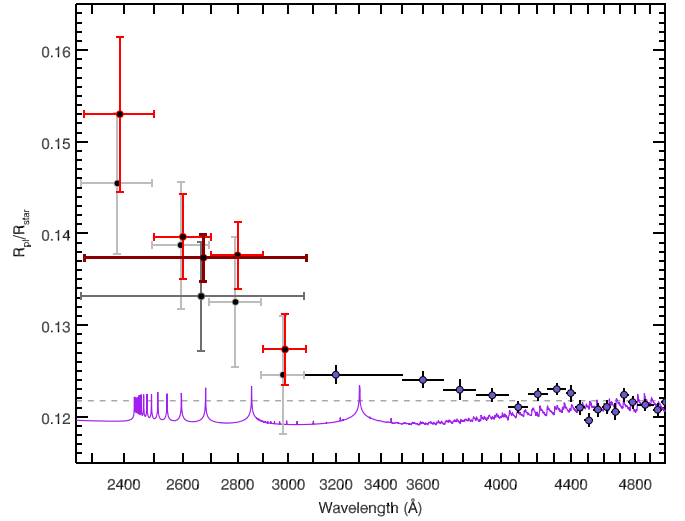

Figure 6. STIS E230M NUV spectra of WASP-121b compared to the optical transmission spectrum. Plotted (red) is the broadband transmission spectra from visit 98 as well as the white-light-curve value (dark red). The NUV broadband spectrum from visit 97 is also plotted (gray) along with the white-light-curve value (dark gray). The optical spectra are also shown (blue) along with a lower atmospheric model from Evans et al. (2018) covering ∼mbar pressures (purple) which was fit to the spectra longward of 4700 Å. The average optical to near-infrared (OIR) value of $R_{\mathrm{pl}}(\mathrm{OIR})/R_{\mathrm{star}} = 0.1217$ is shown by the dashed horizontal line.

For Fe I, there are strong ground-state transitions in the NUV region at wavelengths of 2484, 2523, 2719, 2913, and 2937 Å. While a significant absorption feature does appear near 2484 Å (see Figure 8), the other transitions of Fe I do not obviously appear in the data.

4.7. 1D Transmission Spectra Model

To help further identify absorption features, we fit a 1D analytic transmission spectral model to the data (Lecavelier des Etangs et al. 2008), following the procedures as detailed in Sing et al. (2015) and Sing (2018). Formally, the analytic model is isothermal and assumes a hydrostatic atmosphere with a constant surface gravity with altitude. These assumptions are not expected to be valid over the large altitude ranges probed by the NUV data, especially at very high altitudes. However, the model is useful for identifying spectral features in the transmission spectra, ruling out absorption by different species, and getting a zeroth-order handle on the atmospheric properties, including the velocity. A more comprehensive and physically motivated modeling effort will be presented in a future work (P. Lavvas et al. 2019, in preparation).

To model the transmission spectra, a continuum slope was included, which was assumed to have cross-section opacity with a power law of index α, $(\sigma(\lambda) = \sigma_0(\lambda/\lambda_o)^{-\alpha})$. We also included the spectral lines of Mg I, Mg II, Fe I, and Fe II with the wavelength-dependent cross-sections calculated using the NIST Atomic Spectra Database (Kramida et al. 2018). Voigt profiles were used to broaden the spectral lines. Given our transmission spectra are at very high altitudes, we did not include effects such as collisional broadening and chose instead to fit for the damping parameter governing the line broadening. We calculated the scale height assuming a mean molecular weight corresponding to atomic hydrogen and fit the model using an isothermal temperature. We also assumed that the number of atoms existing in the various atomic levels for a
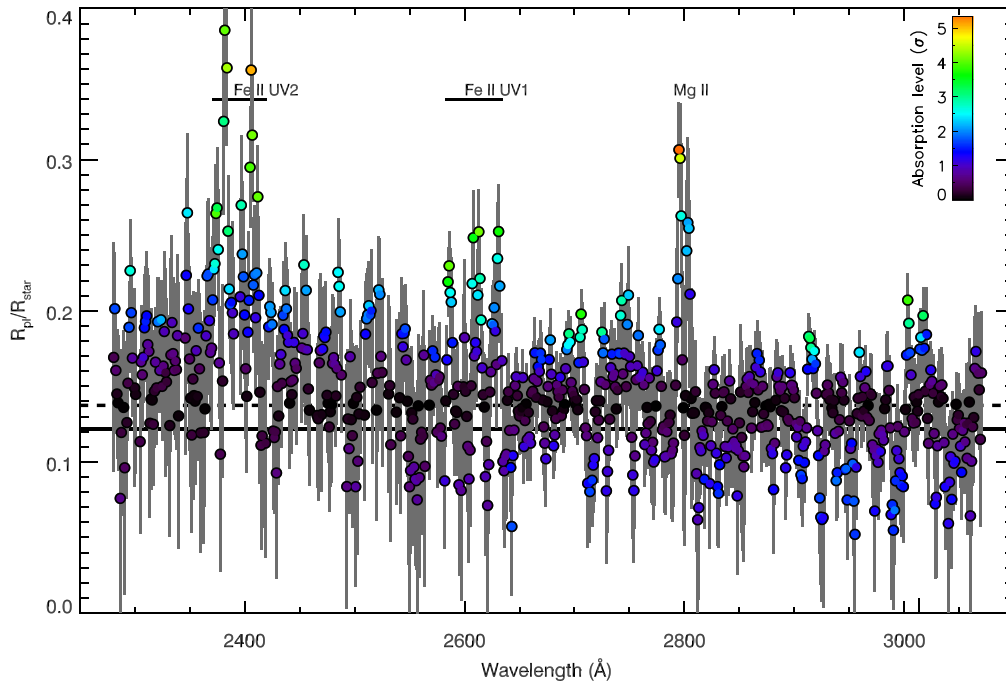
Figure 7. WASP-121b NUV transmission spectrum scanned in 4 Å passbands, with a 1 Å wavelength shift between each adjacent point. The data points have been colored with the significance in transit depth above/below that of the NUV broadband value, which is indicated by the dashed line at $R_{\rm pl}({\rm NUV})/R_{\rm star} = 0.1374$. The average OIR value of $R_{\rm pl}({\rm OIR})/R_{\rm star} = 0.1217$ is shown by the solid black line.

given species followed a Boltzmann distribution with the statistical weights given in the NIST database, though this assumption may not be accurate at very low pressures. To simplify the calculation, we only included transitions where the lower energy level was beneath a threshold. High energy levels will in practice not be sufficiently populated to produce significant absorption signatures, and for Fe II we found transitions above 0.43 eV (corresponding to 5000 K) were not prevalent in the data. However, the excited states of Fe II up to 0.43 eV were needed, as including only ground-state transitions resulted in a much worse fit to the data. The presence of these excited states indicates high temperatures, as a significant population of Fe atoms are found above the ground state.

We fit the model to the NUV data with an L-M least-squares algorithm and MCMC (Eastman et al. 2013). The fit contained five free parameters: the isothermal temperature, α, the Doppler velocity of the planetary atmosphere, the reference planet radius, and the Mg and Fe abundances. We fit for the data between 2300 and 2900 Å, finding a good fit with a χ^2 of 130.4 for 126 dof. We estimate the detection significance of Fe II by excluding its opacity from the model and refitting, finding the χ^2 increases by a $\Delta\chi^2 = 61.8$, which corresponds to a 7.9σ detection significance. The velocity of the planetary atmospheric Mg and Fe lines is measured to be -56^{+43}_{-63} km s^{-1}. Given the velocity uncertainties are larger than the spectrograph resolution, the uncertainties can likely be improved using different data reduction methods (e.g., smaller bins or using cross-correlation techniques), which will be presented in a future work (P. Lavvas et al. 2019, in preparation).

5. Discussion

5.1. Constraints on the Deep Interior

A relatively cold planet interior can lead to the condensing of refractory species deep in the atmosphere, thereby removing the gaseous species from the upper layers of the atmosphere,

trapping them within condensate clouds at depth (Hubeny et al. 2003; Fortney et al. 2008; Powell et al. 2018), a process that is dependent upon particle settling in the presence of turbulent and molecular diffusion (Spiegel et al. 2009; Koskinen et al. 2013). Al, Ti, VO, Fe, and Mg are among the first refractory species to condense out of a hot-Jupiter atmosphere (Visscher et al. 2010; Wakeford et al. 2017). As such, the presence or absence of these species can then provide constraints to the temperatures of the deeper layers for hot Jupiters, as the presence of these elements in the gas phase of the upper layers limits the global temperature profile to be hotter than the condensation of these species. For WASP-121b, the NUV transmission spectrum provides evidence for Mg and Fe in the exosphere, while the optical transmission spectrum shows signatures of VO but a lack of TiO (Evans et al. 2018). The presence of Fe can provide contraints on the interior temperature, $T_{\rm int}$, as the element condenses at the highest temperatures for pressures above about 100 bar (see Wakeford et al. 2017).

We explore the constraints on the deep interior temperature (pressures $\gtrsim 10$ bar) using the best-fit retrieved temperature–pressure (T–P) profile for WASP-121b, derived from fitting the dayside emission spectra of Evans et al. (2017), which is sensitive to approximately bar to mbar pressure levels and has recently been updated to include *HST* WFC3 G102 and *Spitzer* data (Mikal-Evans et al. 2019). The T–P profile was generated using the analytical model of Guillot (2010), which assumes radiative equilibrium, and is parameterized with the Planck mean thermal infrared opacity, $\kappa_{\rm IR}$, the ratio of the optical-to-infrared (OIR) opacity, γ, an irradiation efficiency factor β, and the interior temperature of the planet, $T_{\rm int}$. Emission spectra are not directly sensitive to $T_{\rm int}$ (Line et al. 2013b), so retrievals often do not probe the deep interior pressure layers and fix $T_{\rm int}$, with Evans et al. (2017; see also Mikal-Evans et al. 2019) setting $T_{\rm int}$ to Jupiter-like 100 K values. However, with both
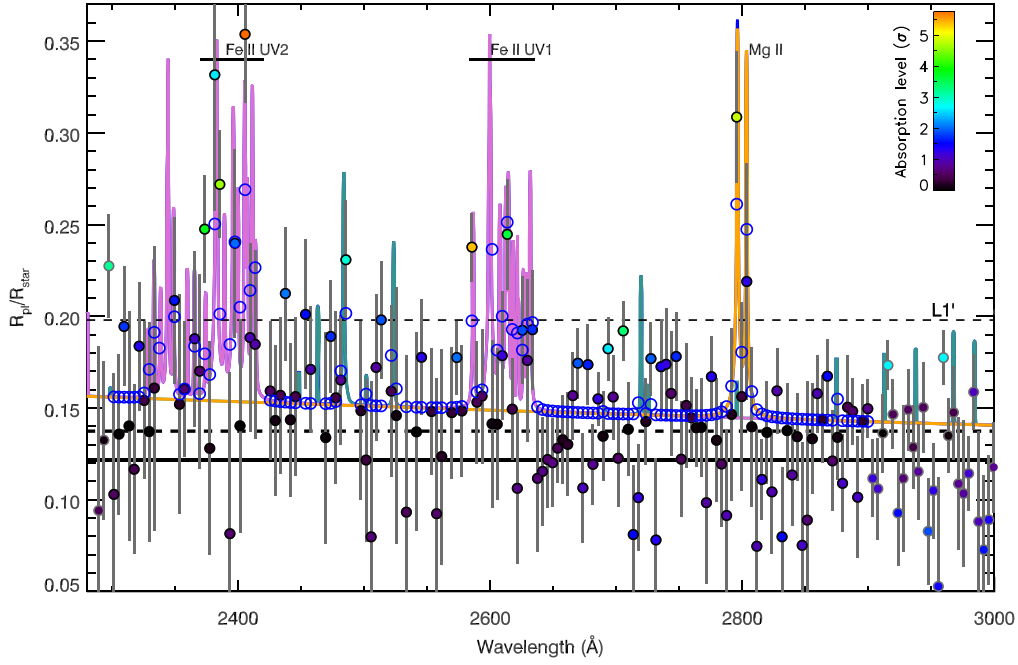
Figure 8. WASP-121b NUV transmission spectrum in unique 4 Å passbands. The data points have been colored with the significance in transit depth above that of the NUV spectrum, which is indicated by the black dashed line at $R_{pl}(NUV)/R_{star} = 0.1374$. A model fit that includes Fe I (green), Fe II (purple), and Mg II (orange) absorption is shown, with the complete model integrated over the spectral passband shown with (blue) open circles. The Lagrange point distance L1' is also indicated.
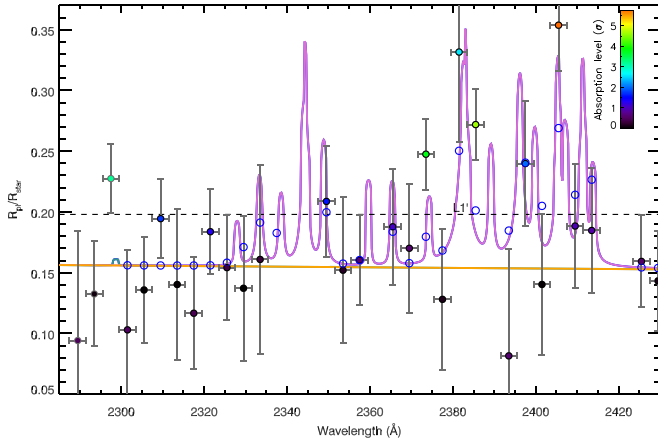
Figure 9. Same as Figure 8 but zoomed in over the Fe II UV2 region. Points have been removed in spectral regions with strong stellar absorption lines, where the transit itself has not been detected due to low signal-to-noise.

Figure 11. Same as Figure 8 but zoomed in over the Mg II region.

Mg and Fe present in the upper layers of the atmosphere, temperatures of $T_{int} = 100$ K are clearly too low, as the T–P profile intersects Fe and Mg condensation curves at high pressures (see Figure 13). As the condensation curves are metallicity dependent (Visscher et al. 2010; Wakeford et al. 2017), we illustrate the constraints in Figure 13 using $10\times$ solar metallicity, which is close to the best-fit retrieved abundances for WASP-121b in both the transmission and emission spectra (Evans et al. 2017, 2018; see also Mikal-Evans et al. 2019). Varying T_{int} in steps of 100 K and using the best-fit T–P profile parameters ($\kappa_{IR} = 0.0049$ cm^2 g^{-1}, $\gamma = 4.08$, $\beta = 1.03$), we find internal temperatures near $T_{int} = 500$ K are needed to prevent both Fe and Mg from condensing deep in the atmosphere, but this also allows TiO to condense at pressures well below the photosphere. As discussed in Fortney et al. (2008), for adiabatic interiors higher values of T_{int} lead to warmer interiors and larger planet radii. Given WASP-121b is one of the largest exoplanets found ($R_{pl} = 1.865 R_{Jup}$; Delrez et al. 2016), a high T_{int} would be expected.

Figure 10. Same as Figure 8 but zoomed in over the Fe II UV1 region.
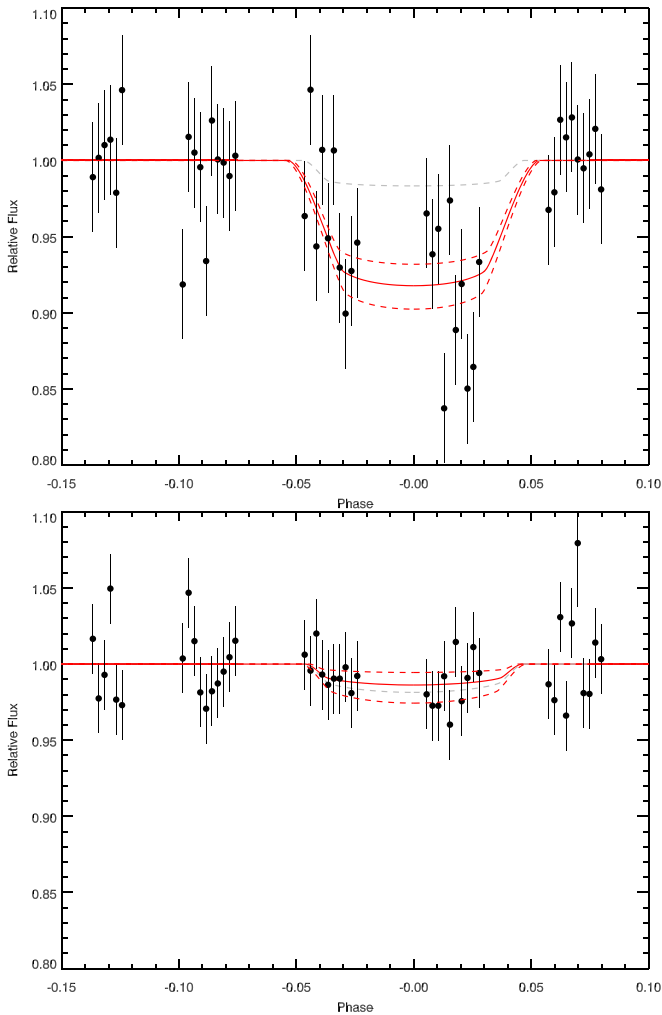
Figure 12. Transit light curves for 10 Å wide passbands, corrected for systematic errors. Top: a light curve composed of two 5 Å bins centered directly on the Mg II doublet, which optimally covers the two lines. Bottom: a light-curve composed of two 5 Å bands placed adjacent to either side of the Mg II centered bands, which samples the nearby continuum. In both plots the average OIR radius is shown as the gray dashed lines. The red lines show the best-fit transit depths (solid) and the depths covering the 1σ uncertainties (dashed).

While there are computational limitations, we note that self-consistent 3D modeling efforts that include both the deep interior and the exosphere in comparison to transmission, emission, and phase curve data can provide better constraints on the irradiation efficiency, atmospheric abundances, atmospheric mixing, and global T–P profiles, which in turn would provide the best condensation constraints on T_{int}.

5.2. Roche Lobe Geometry and Exospheric Constraints

The ionized Mg and Fe lines are seen up to extremely high altitudes, corresponding to high planetary radii of $R_{pl}/R_{star} \sim 0.3$. We compare the altitudes of this absorption material to the theoretical distances of the L1 Lagrange point, D_{L1}, and the L1' Lagrange point, $D_{L1'}$, which is the distance between the planet's center and the closest point of the equipotential surface including L1, which is the Roche lobe. Using the formalism in Gu et al. (2003) and using a mass ratio of $M_{pl}/(M_{pl} + M_{star}) = 8.3 \times 10^{-4}$ as well as $a/R_{star} = 3.76$, we calculate $D_{L1}/R_{star} = 0.24$ (or $1.96R_{pl}$) and the L1' Lagrange size relative to that of the star to be

$D_{L1'}/R_{star} = 0.209$ (or $1.72R_{pl}$). In a transit configuration, the observed limit of the Roche lobe is perpendicular to the planet–star direction and the Roche lobe extends to about 2/3 of the extension to the L1 Lagrange point (Vidal-Madjar et al. 2008). For WASP-121b, we numerically calculated the equivalent radius[21] of a transiting Roche lobe, R_{eqRL}, finding $R_{eqRL}/R_{star} = 0.158$ (or $1.3\,R_{pl}$).

The core of the Mg II k line reaches up to $R_{pl}/R_{star} = 0.309 \pm 0.036$ (or $2.52 \pm 0.29R_{pl}$), which is in excess of R_{eqRL}/R_{star} at 4σ confidence. In addition, the ground-state Fe II resonance line at 2382 Å reaches up to $R_{pl}/R_{star} = 0.331 \pm 0.074$ (or $2.7 \pm 0.6R_{pl}$), which is in excess of R_{eqRL}/R_{star} at 2.7σ confidence. In a transit configuration, these absorption features indicate that both Mg II and Fe II reach altitudes such that they are no longer gravitationally bound to the planet. While large hydrogen tails extending well beyond the Roche lobe have been seen at Lyα (Ehrenreich et al. 2015; Bourrier et al. 2018), elements heavier than hydrogen in exoplanets have not previously been found at distances in excess of the Roche lobe.

The existence of heavy atmospheric material reaching beyond the Roche lobe agrees with a geometric blow-off scenario (Lecavelier des Etangs et al. 2004), where the Roche lobe is in close spatial proximity to the planet and the exobase can extend beyond it, letting atmospheric gas freely stream away from the planet. WASP-121b is an ideal planet to potentially observe this phenomenon, as the planet is on the verge of tidal disruption (Delrez et al. 2016). At the terminator, the planet fills a significant portion of its Roche lobe, with the OIR radii reaching $R_{pl}(OIR)/R_{eqRL} = 77\%$. The NUV value reaches $R_{pl}(NUV)/R_{eqRL} = 87 \pm 2\%$, indicating the NUV continuum contains opaque material nearly up to the transit-projected Roche lobe, while the cores of the Mg II and Fe II exceed the Roche lobe. A similar process is likely happening in comparably hot and tidally distorted planets such as WASP-12b, which also shows evidence of Mg II and Fe II absorption (Fossati et al. 2010; Haswell et al. 2012). However WASP-121b has a more favorable transmission spectral signal and orbits a significantly brighter star than WASP-12A. These properties allow the WASP-121b NUV data to be fit at relatively high resolution with a full limb-darkened, instrument-systematic-corrected transit model, which allows the transmission spectral line profiles to be well resolved and absolute transit depths preserved. Our transit light curves cover ingress, though no early ingress is observed as the NUV transit time is in excellent agreement with the expected ephemeris (see Section 4.3). Like WASP-12b (Nichols et al. 2015; Turner et al. 2016), there is no evidence in WASP-121b for a bow shock or material overflowing the L1 Lagrange point (Lai et al. 2010; Vidotto et al. 2010; Llama et al. 2011; Bisikalo et al. 2013).

As ionized species, the Mg II and Fe II atoms are potentially sensitive to the planet's magnetic field, which if strong enough could lead to magnetically controlled outflows (Adams 2011). As such, departures in the transit light curves from spherical symmetry and the velocity profile of the ionized lines could give insights into the nature of the outflow. Our data lack complete phase coverage, so only have a limited ability to constrain a non-spherical absorption profile and we cannot constrain a possible post-transit cometary-like evaporation tail. However, we note that all of our transit light curve fits were

---

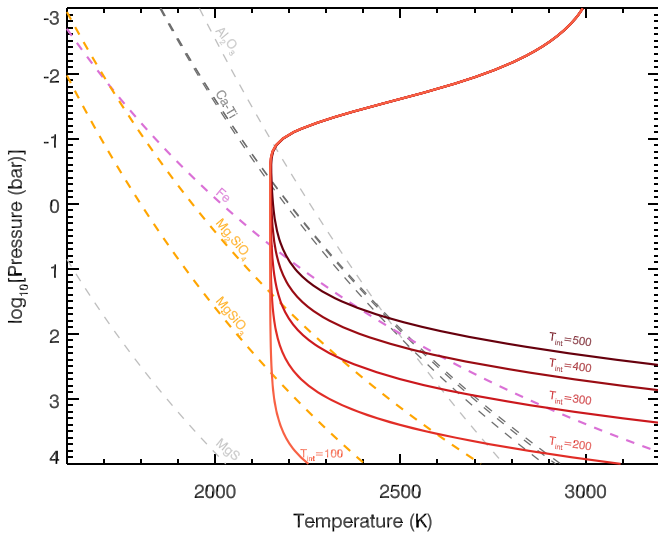[21] Equivalent meaning the radius of a disk with the same area.

Figure 13. Temperature–pressure profiles for WASP-121b (solid lines) compared to condensation curves computed for a metallicity of $10\times$ solar (dashed lines). Interior temperatures from 100 to 500 K are shown.

well fit to near the photon-noise limit assuming the planet was a sphere. In addition, our model fit found velocities of -56^{+43}_{-63} km s^{-1}, which does not have sufficient precision to confidently distinguish between outflowing blueshifted gas or zero-velocity gas.

6. Conclusion

We have presented *HST* NUV transit observations of WASP-121b and introduced a new detrending method, which we find helps improve the photometric performance of time-series *HST* STIS data. WASP-121b is one of the few exoplanets with a complete NUV–OIR transmission spectrum that can be compared on an absolute transit depth scale from NUV wavelengths into the near-infrared. The whole NUV wavelength region shows significant absorption, with transit depths well in excess of the optical and near-infrared levels and an NUV continuum that rises dramatically blueward of about 3000 Å. We find spectral characteristics that have not previously been observed, with strong features of ionized Mg and Fe lines that extend well above the Roche lobe observed, with multiple resolved spectral lines detected for both species. While not gravitationally bound, it is unclear whether these ionized species are magnetically confined to the planet, though better signal-to-noise spectra would improve velocity measurements, and complete phase coverage searching for non-spherical symmetries could provide further insight. The presence of gas beyond the Roche lobe is evidence this tidally distorted planet is undergoing hydrodynamic outflow with a geometric blow-off, where the exobase extends to or exceeds the Roche lobe, and elements heavier than hydrogen are free to escape. Spectrally resolved Mg II and Fe II features on an absolute transit depth scale will allow detailed simulations of the local physical conditions of the upper atmosphere, where it may be possible to deduce the altitude dependent density, temperature, and abundances of the upper atmosphere.

Facilities: HST (STIS), TESS.

Appendix
Benchmarking Jitter Detrending with WASP-12b STIS CCD Eclipse Data

We benchmarked the use of jitter detrending on the STIS G430L eclipse data of WASP-12b to verify the jitter engineering data could be used to detrend and fit STIS transit light-curve data and to compare the performance with the latest methods. A subset of the optical state jitter vectors can be seen in Figure 14 for the 2017 June 15 STIS data. Results from these data have been published in Bell et al. (2017), who used a Gaussian process with the traditional model optical state vectors to model the light curve systematics. In our analysis, the data reduction steps were identical to those of Bell et al. (2017); however, we included the first *HST* orbit in our analysis and discarded the first exposure in each orbit.

We modeled N measured fluxes over time, $f(t)$, as a combination of an eclipse model, $T(t, \delta)$ (which depends upon the eclipse parameter δ), the total baseline flux detected from the star, F_0, and a parameterized systematics error model $S(x)$, giving

$$f(t) = T(t, \theta) \times F_0 \times S(x). \qquad (4)$$

With no ingress or egress measurements in the light curves, as done by Evans et al. (2013) and Bell et al. (2017), we used a boxcar function to describe the eclipse signal, with

$$
\begin{aligned}
T_i &= (1 - \delta B_i) \\
B_i &= \begin{cases} 0 & i \in \text{out of eclipse} \\ 1 & i \in \text{in eclipse,} \end{cases}
\end{aligned}
\qquad (5)
$$

where δ is the fractional flux change during the eclipse for exposure measurements $i = 1, ..., N$. For our systematics error model, we included the traditional optical state vectors (ϕ_{HST}, ϕ_{HST}^2, ϕ_{HST}^3, ϕ_{HST}^4, X_{psf}, Y_{psf}, and S_λ) as well as the jitter vectors *V2_roll*, *V3_roll*, *R.A.*, *decl.*, *Lat*, *Long*, such that the most complex model contained 13 terms used to describe $S(x)$. We included only linear terms for all of the optical state vectors aside from ϕ_{HST}, which was fit up to fourth order. Higher-order

13

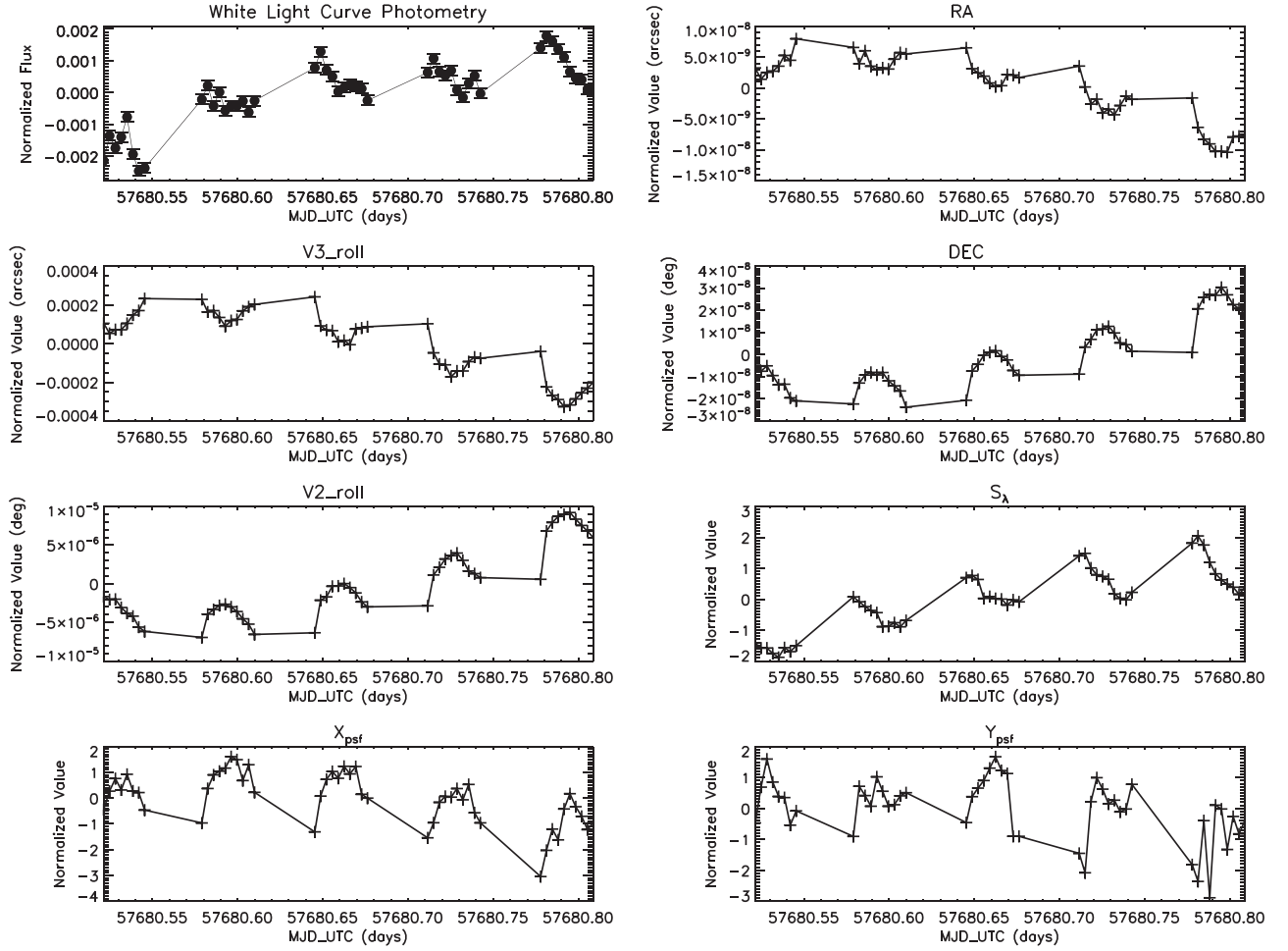**Figure 14.** White-light curve of WASP-12b and selected jitter engineering measurements ($V3_{roll}$, $V3_{roll}$, $R.A.$, and $decl.$) for visit 3. Several traditional detrending variables (X_{psf}, Y_{psf}, and S_λ) are shown as well.

terms in the remaining the parameters were explored but found not to improve the fits. With a $f(t)$ containing only linear parametrized terms, including the eclipse model, we used a multiple linear regression fit to find the best-fit parameters and 1σ uncertainly estimates (Bevington & Robinson 2003). For the systematics error models, we fit the light-curves using all combinations of the 13 optical state vectors terms for $S(x)$ giving $2^{13} = 8192$ total fits to the data for each *HST* visit. By fitting all combinations, our model includes not only the traditional decorrelation parameters but models with jitter vectors as well. Rather than selecting only the best-fitting light curve, we used the marginalization method as described in Gibson (2014) to incorporate the uncertainty in the choice of the systematics model into the eclipse depth measurement. This method has been shown to be effective for WFC3 data (Wakeford et al. 2016) and has also been used for STIS data (Lothringer et al. 2018). For all 8192 systematics models, we approximate the evidence, E_q, using the second-order AICc:

$$E_q \approx -\frac{1}{2}\text{AICc}$$

$$\text{AICc} = \text{AIC} + \frac{2k^2 + 2k}{n - k - 1}, \qquad (6)$$

where N denotes the number of measurements in the light curve and k denotes the number of fit parameters. The AICc applies a correction for small sample sizes to the AIC, and so helps to address potential overfitting problems in the case when N is small, as can be the case in these data. Photon noise error bars were initially assumed when fitting the light curves, and the measured parameters were then rescaled based on the standard deviation of the light curve residuals.

The vector pairs ($V2\_roll$, $V3\_roll$) and ($R.A.$, $decl.$) often exhibit very similar trends. In practice, including multiple vectors with the same (if not identical) trends could bias the model-averaged results when marginalizing, as it can result in over-counting the common trends contained in the vectors, and detrending with multiple similar optical vectors will introduce large fitting degeneracies. Our main objective here was to allow the fitting to use any combination of optical state vectors to directly test the performance of the jitter optical state vectors against the traditional vectors, so we chose to include all vectors in our study rather than select unique vectors. However, to help mitigate the aforementioned shortcomings, we used principal component analysis (PCA) to convert the vector pairs into a set of orthogonal vectors, which were then subsequently used to fit the light curves. This additional PCA procedure helped to reduce fitting degeneracies between highly correlated
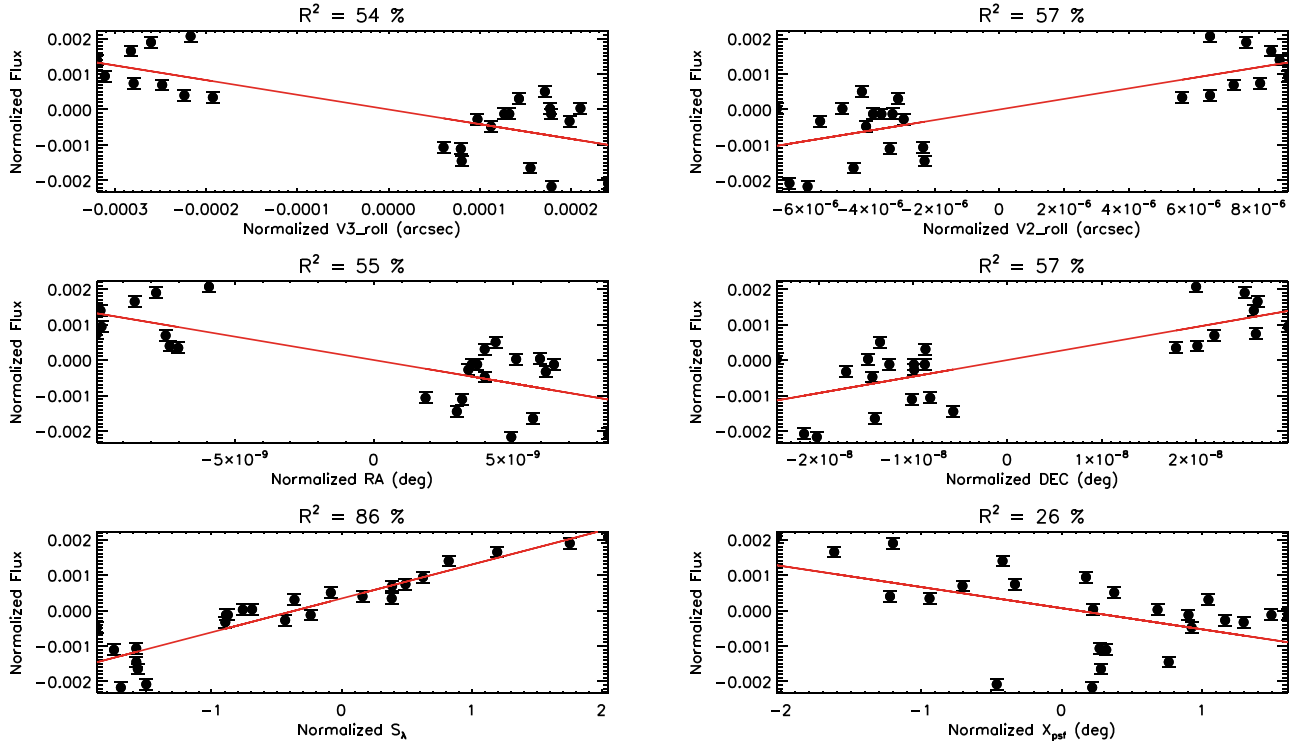
Figure 15. Correlations between the WASP-12b out-of-eclipse white-light-curve data and several optical-state jitter vectors. A linear trend (red) and R^2 correlation values are also shown.
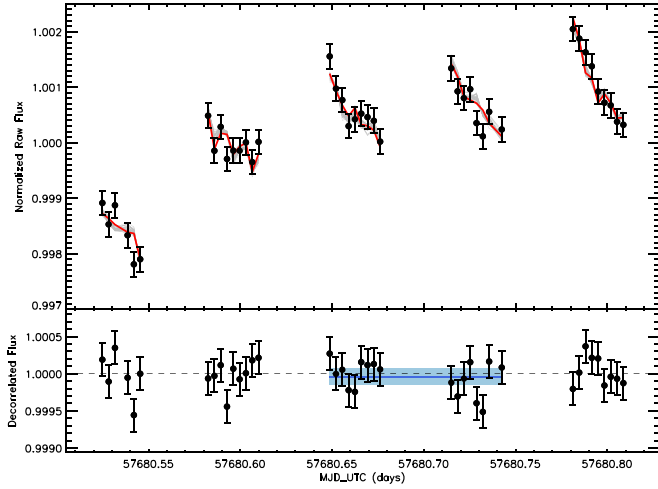

Figure 16. Top: raw light-curve time-series flux of WASP-12b. The top-fitting model is shown in red, and models with weights larger than 0.5% are also shown in gray. Bottom: detrended light curve; the dark blue line indicates the top-fitting model eclipse depth and the 1σ uncertainty is indicated by the light blue bar.

**Figure 17.** Marginalized eclipse depth results showing models with weights over 0.5%.

jitter-vector pairs and also helped effectively reduce the number of jitter vectors that were included in the our best-fitting models.

Our best fit to the white-light-curve data achieved a precision of 70% of the theoretical photon noise limit with standard deviations of 218 ppm (see Figures 15, 16, and 17). The best-fitting systematics models included the jitter detrending optical state vectors *V2_roll*, *V3_roll*, *decl.*, *Lat*, and *Long*. For the broadband eclipse depth, we measured a model-marginalized eclipse depth of $\delta = 59 \pm 134$, which is compatible within the errors to that of Bell et al. (2017) who reported $\delta = -53 \pm 74$. As noted by Bell et al., the measured eclipse depth should be strictly positive, though in practice it may be negative due to either random or systematic noise. With jitter detrending, the first orbit was successfully recovered for use in the analysis, and we found the measured eclipse depth is positive. The eclipse depth translates to a measured geometric albedo of ($A_g = 3.9 \pm 8.8\%$), which is very low and in agreement with the findings of Bell et al. (2017). Thus, with this test and the

results of Section 2.1, we conclude the jitter products of the EDPS generally contain sufficiently accurate information to help decorrelate precision time-series spectrophotometry.

ORCID iDs

David K. Sing ⓘ https://orcid.org/0000-0001-6050-7645
Panayotis Lavvas ⓘ https://orcid.org/0000-0002-5360-3660
Mark S. Marley ⓘ https://orcid.org/0000-0002-5251-2943
Nikolay Nikolov ⓘ https://orcid.org/0000-0002-6500-3574
Lotfi Ben-Jaffel ⓘ https://orcid.org/0000-0003-4047-2793
Vincent Bourrier ⓘ https://orcid.org/0000-0002-9148-034X
Lars A. Buchhave ⓘ https://orcid.org/0000-0003-1605-5666
David Ehrenreich ⓘ https://orcid.org/0000-0001-9704-5405
Thomas Mikal-Evans ⓘ https://orcid.org/0000-0001-5442-1300
Tiffany Kataria ⓘ https://orcid.org/0000-0003-3759-9080
Nikole K. Lewis ⓘ https://orcid.org/0000-0002-8507-1304
Mercedes López-Morales ⓘ https://orcid.org/0000-0003-3204-8183
Antonio García Muñoz ⓘ https://orcid.org/0000-0003-1756-4825
Gregory W. Henry ⓘ https://orcid.org/0000-0003-4155-8513
Jorge Sanz-Forcada ⓘ https://orcid.org/0000-0002-1600-7835
Hannah R. Wakeford ⓘ https://orcid.org/0000-0003-4328-3867

References

Adams, F. C. 2011, ApJ, 730, 27
Ballester, G. E., & Ben-Jaffel, L. 2015, ApJ, 804, 116
Bell, T. J., Nikolov, N., Cowan, N. B., et al. 2017, ApJL, 847, L2
Ben-Jaffel, L. 2007, ApJL, 671, L61
Ben-Jaffel, L. 2008, ApJ, 688, 1352
Ben-Jaffel, L., & Ballester, G. E. 2013, A&A, 553, A52
Ben-Jaffel, L., & Ballester, G. E. 2014, ApJL, 785, L30
Berta, Z. K., Charbonneau, D., Désert, J.-M., et al. 2012, ApJ, 747, 35
Bevington, P. R., & Robinson, D. K. 2003, Data Reduction and Error Analysis for the Physical sciences (New York: McGraw-Hill)
Bisikalo, D., Kaygorodov, P., Ionov, D., et al. 2013, ApJ, 764, 19
Bourrier, V., Lecavelier des Etangs, A., Ehrenreich, D., et al. 2018, A&A, 620, A147
Brown, T. M., Charbonneau, D., Gilliland, R. L., Noyes, R. W., & Burrows, A. 2001, ApJ, 552, 699
Cauley, P. W., Shkolnik, E. L., Ilyin, I., et al. 2019, AJ, 157, 69
Delrez, L., Santerne, A., Almenara, J.-M., et al. 2016, MNRAS, 458, 4025
Deming, D., & Sheppard, K. 2017, ApJL, 841, L3
Demory, B.-O., Ehrenreich, D., Queloz, D., et al. 2015, MNRAS, 450, 2043
Eastman, J., Gaudi, B. S., & Agol, E. 2013, PASP, 125, 83
Eastman, J., Siverd, R., & Gaudi, B. S. 2010, PASP, 122, 935
Ehrenreich, D., Bourrier, V., Wheatley, P. J., et al. 2015, Natur, 522, 459
Evans, T. M., Pont, F., Sing, D. K., et al. 2013, ApJL, 772, L16
Evans, T. M., Sing, D. K., Goyal, J. M., et al. 2018, AJ, 156, 283
Evans, T. M., Sing, D. K., Kataria, T., et al. 2017, Natur, 548, 58
Evans, T. M., Sing, D. K., Wakeford, H. R., et al. 2016, ApJL, 822, L4
Fortney, J. J., Lodders, K., Marley, M. S., & Freedman, R. S. 2008, ApJ, 678, 1419
Fossati, L., Ayres, T. R., Haswell, C. A., et al. 2013, ApJL, 766, L20
Fossati, L., Haswell, C. A., Froning, C. S., et al. 2010, ApJL, 714, L222
Gaia Collaboration, Brown, A. G. A., Vallenari, A., et al. 2018, A&A, 616, A1
García Muñoz, A. 2007, P&SS, 55, 1426
Gaudi, B. S., Stassun, K. G., Collins, K. A., et al. 2017, Natur, 546, 514
Gibson, N. P. 2014, MNRAS, 445, 3401
Gibson, N. P., Nikolov, N., Sing, D. K., et al. 2017, MNRAS, 467, 4591
Gibson, N. P., Pont, F., & Aigrain, S. 2011, MNRAS, 411, 2199
Gu, P.-G., Lin, D. N. C., & Bodenheimer, P. H. 2003, ApJ, 588, 509

Guillot, T. 2010, A&A, 520, A27
Haswell, C. A., Fossati, L., Ayres, T., et al. 2012, ApJ, 760, 79
Hoeijmakers, H. J., Ehrenreich, D., Heng, K., et al. 2018, Natur, 560, 453
Hoeijmakers, H. J., Ehrenreich, D., Kitzmann, D., et al. 2019, arXiv:1905.02096
Hubeny, I., Burrows, A., & Sudarsky, D. 2003, ApJ, 594, 1011
Huitson, C. M., Sing, D. K., Pont, F., et al. 2013, MNRAS, 434, 3252
Jenkins, J. M., Twicken, J. D., McCauliff, S., et al. 2016, Proc. SPIE, 9913, 99133E
Jensen, A. G., Cauley, P. W., Redfield, S., Cochran, W. D., & Endl, M. 2018, AJ, 156, 154
Koskinen, T. T., Yelle, R. V., Harris, M. J., & Lavvas, P. 2013, Icar, 226, 1695
Kramida, A., Ralchenko, Yu., Reader, J. & NIST ASD Team 2018, NIST Atomic Spectra Database (ver. 5.6.1) (Gaithersburg, MD: NIST), https://physics.nist.gov/asd
Lai, D., Helling, C., & van den Heuvel, E. P. J. 2010, ApJ, 721, 923
Lavie, B., Ehrenreich, D., Bourrier, V., et al. 2017, A&A, 605, L7
Lecavelier des Etangs, A., Bourrier, V., Wheatley, P. J., et al. 2012, A&A, 543, L4
Lecavelier Des Etangs, A., Ehrenreich, D., Vidal-Madjar, A., et al. 2010, A&A, 514, A72
Lecavelier des Etangs, A., Pont, F., Vidal-Madjar, A., & Sing, D. 2008, A&A, 481, L83
Lecavelier des Etangs, A., Vidal-Madjar, A., McConnell, J. C., & Hébrard, G. 2004, A&A, 418, L1
Line, M. R., Knutson, H., Deming, D., Wilkins, A., & Desert, J.-M. 2013a, ApJ, 778, 183
Line, M. R., Wolf, A. S., Zhang, X., et al. 2013b, ApJ, 775, 137
Linsky, J. L., Yang, H., France, K., et al. 2010, ApJ, 717, 1291
Llama, J., Wood, K., Jardine, M., et al. 2011, MNRAS, 416, L41
Lothringer, J. D., Benneke, B., Crossfield, I. J. M., et al. 2018, AJ, 155, 66
Magic, Z., Chiavassa, A., Collet, R., & Asplund, M. 2015, A&A, 573, A90
Mandel, K., & Agol, E. 2002, ApJL, 580, L171
Markwardt, C. B. 2009, in ASP Conf. Ser. 411, Astronomical Data Analysis Software and Systems XVIII, ed. D. A. Bohlender, D. Durand, & P. Dowler (San Francisco, CA: ASP), 251
Mikal-Evans, T., Sing, D. K., Goyal, J. M., et al. 2019, MNRAS, 488, 2222
Murray-Clay, R. A., Chiang, E. I., & Murray, N. 2009, ApJ, 693, 23
Nichols, J. D., Wynn, G. A., Goad, M., et al. 2015, ApJ, 803, 9
Nikolov, N., Sing, D. K., Pont, F., et al. 2014, MNRAS, 437, 46
Owen, J. E., & Jackson, A. P. 2012, MNRAS, 425, 2931
Pont, F., Zucker, S., & Queloz, D. 2006, MNRAS, 373, 231
Powell, D., Zhang, X., Gao, P., & Parmentier, V. 2018, ApJ, 860, 18
Salz, M., Schneider, P. C., Fossati, L., et al. 2019, A&A, 623, A57
Sing, D. K. 2010, A&A, 510, A21
Sing, D. K. 2018, arXiv:1804.07357
Sing, D. K., Fortney, J. J., Nikolov, N., et al. 2016, Natur, 529, 59
Sing, D. K., Lecavelier des Etangs, A., Fortney, J. J., et al. 2013, MNRAS, 436, 2956
Sing, D. K., Pont, F., Aigrain, S., et al. 2011, MNRAS, 416, 1443
Sing, D. K., Wakeford, H. R., Showman, A. P., et al. 2015, MNRAS, 446, 2428
Spiegel, D. S., Silverio, K., & Burrows, A. 2009, ApJ, 699, 1487
Stumpe, M. C., Smith, J. C., Van Cleve, J. E., et al. 2012, PASP, 124, 985
Turner, J. D., Pearson, K. A., Biddle, L. I., et al. 2016, MNRAS, 459, 789
Vidal-Madjar, A., Désert, J.-M., Lecavelier des Etangs, A., et al. 2004, ApJL, 604, L69
Vidal-Madjar, A., Huitson, C. M., Bourrier, V., et al. 2013, A&A, 560, A54
Vidal-Madjar, A., Lecavelier des Etangs, A., Désert, J.-M., et al. 2003, Natur, 422, 143
Vidal-Madjar, A., Lecavelier des Etangs, A., Désert, J.-M., et al. 2008, ApJL, 676, L57
Vidotto, A. A., Jardine, M., & Helling, C. 2010, ApJL, 722, L168
Visscher, C., Lodders, K., & Fegley, B., Jr. 2010, ApJ, 716, 1060
Wakeford, H. R., Sing, D. K., Deming, D., et al. 2013, MNRAS, 435, 3481
Wakeford, H. R., Sing, D. K., Evans, T., Deming, D., & Mandell, A. 2016, ApJ, 819, 10
Wakeford, H. R., Visscher, C., Lewis, N. K., et al. 2017, MNRAS, 464, 4247
Yan, F., & Henning, T. 2018, NatAs, 2, 714
Yelle, R. V. 2004, Icar, 170, 167